Research
A SCIENCE PARTNER JOURNAL

RESEARCH ARTICLE

Light-Triggered Graphene/Black Phosphorus Heterostructure FET Platform for Ultrasensitive Detection of Alzheimer's Disease Biomarkers at the Zeptomole Level

Huide Wang[1†], Meng Qiu[2†], Chen Wang[2†], Liding Zhang[3,4], Ning Fan[5], Zhi Chen[1,6], Yi Liu[1], Tianzhong Li[1], Ziqian Wang[1], Yihan Zhu[1], Yule Zhang[1], Xilin Tian[1], Yun Wang[5], Mingmin Yang[5], Dianyuan Fan[1], Qingming Luo[4,7], Ke Jiang[8], Haiming Luo[3,4,7*], and Han Zhang[1,9*]

[1]State Key Laboratory of Radio frequency Heterogeneous integration, International Collaborative Laboratory of 2D Materials for Optoelectronics Science and Technology, Institute for Advanced Study in Nuclear Energy & Safety, Interdisciplinary Center of High Magnetic Field Physics of Shenzhen University, College of Physics and Optoelectronic Engineering, Shenzhen University, Shenzhen, China. [2]Key Laboratory of Marine Chemistry Theory and Technology (Ministry of Education), College of Chemistry and Chemical Engineering, Ocean University of China, Qingdao, China. [3]Britton Chance Center for Biomedical Photonics, Wuhan National Laboratory for Optoelectronics, MoE Key Laboratory for Biomedical Photonics, Huazhong University of Science and Technology, Wuhan, China. [4]State Key Laboratory of Digital Medical Engineering, Key Laboratory of Biomedical Engineering of Hainan Province, School of Biomedical Engineering, Hainan University, Haikou, China. [5]Shenzhen Eye Hospital, Shenzhen Eye Medical Center, Southern Medical University, Shenzhen 518040, China. [6]Department of Chemistry, Korea University, Seoul, South Korea. [7]Research Unit of Multimodal Cross Scale Neural Signal Detection and Imaging, Chinese Academy of Medical Sciences, HUST-Suzhou Institute for Brainsmatics, JITRI, Suzhou, China. [8]State Key Laboratory of Luminescence and Applications, Changchun Institute of Optics, Fine Mechanics and Physics, Chinese Academy of Sciences, Changchun, China. [9]Key Laboratory of Organosilicon Chemistry and Material Technology (Ministry of Education), College of Material Chemistry and Chemical Engineering, Hangzhou Normal University, Hangzhou, China.

*Address correspondence to: hemluo@hust.edu.cn (H.L.); hzhang@szu.edu.cn (H.Z.)
†These authors contributed equally to this work.

Citation: Wang H, Qiu M, Wang C, Zhang L, Fan N, Chen Z, Liu Y, Li T, Wang Z, Zhu Y, et al. Light-Triggered Graphene/Black Phosphorus Heterostructure FET Platform for Ultrasensitive Detection of Alzheimer's Disease Biomarkers at the Zeptomole Level. *Research* 2025;8:Article 0772. https://doi.org/10.34133/research.0772

Submitted 20 November 2024
Revised 11 June 2025
Accepted 14 June 2025
Published 14 August 2025

Copyright © 2025 Huide Wang et al. Exclusive licensee Science and Technology Review Publishing House. No claim to original U.S. Government Works. Distributed under a Creative Commons Attribution License (CC BY 4.0).

Due to the low concentration of amyloid-beta (Aβ) in plasma and the high content of interfering factors, the conventional detection method for the quantification of Aβ still faces the problem of insufficient limit of detection (LOD). In this work, we propose a new light-triggered graphene–black phosphorus heterostructure (G-BP) field-effect transistor (FET) biosensing platform that achieves a marked reduction in the LOD. The LOD for Alzheimer's disease (AD) biomarker $A\beta_{42}$ detection using the G-BP FET is as low as 235.1 zM (2.351×10^{-19} M), which is the lowest value reported to date and is approximately 2 to 3 orders of magnitude lower than other reported biosensing platforms. The G-BP FET platform provides precise, real-time guidance for non-invasive early diagnosis, disease monitoring, and personalized treatment plans for AD. Moreover, this method has good scalability and potential applications in other areas, including early detection of cancer and other major chronic diseases.

Introduction

Alzheimer's disease (AD) is characterized by progressive neuropathology and brain atrophy, affecting over 50 million individuals, with projections indicating that this number will reach approximately 152 million by 2050 [1,2]. Amyloid-beta (Aβ) plaques and neurofibrillary tangles (NFTs) composed of phosphorylated tau (p-tau) are widely recognized as the hallmark pathological changes of AD. Among these, aggregated Aβ exhibits critical neurotoxic effects, leading to dendritic retraction and

neuronal degeneration, ultimately resulting in memory impairment [3–7]. The primary Aβ subtypes are $A\beta_{40}$ and $A\beta_{42}$, with $A\beta_{42}$ being more prone to fibrillization and demonstrating a stronger tendency for aggregation [2]. The effectiveness of AD treatment depends on how early the treatment is started [8,9]. Therefore, there is an urgent need to develop screening methods that can accurately detect the early stages of AD. In recent decades, biomarker-based non-imaging diagnostic methods utilizing cerebrospinal fluid (CSF), including techniques such as enzyme-linked immunosorbent assay [10,11], nanoparticle-based immunoassays [12], surface-enhanced Raman spectroscopy [13,14], fluorescence biosensors [15], and electrochemical biosensors [16–18], have promoted the development of early diagnosis technology for brain diseases. Recently, minimally invasive detection techniques based on blood biomarkers have received attention, due to better patient compliance and ease for clinical translation. However, the complexity of substances and the presence of numerous interfering signals in blood, coupled with the blood–brain barrier that leads to markedly lower concentrations of biomarkers such as Aβ in blood compared to CSF, pose challenges for traditional detection methods when applied to the detection of blood-based biomarkers. For instance, the limit of detection (LOD) and specificity may not meet the necessary requirements [19,20]. Despite these limitations, plasma $A\beta_{42}$ levels and the $A\beta_{42}/A\beta_{40}$ ratio have demonstrated substantial clinical relevance, correlating with cerebral amyloid deposition and serving as predictive indicators of cognitive decline in cohort studies [21–23]. Critically, blood-based $A\beta_{42}$ assays achieve reliable detection during the preclinical and mild cognitive impairment stages of AD, enabling timely intervention before symptom onset [24]. Furthermore, most of the $A\beta_{42}$ in blood exists as monomers, making monomer-targeted detection clinically feasible and essential for minimizing false negatives in early screening [25].

Biosensors based on field-effect transistors (FETs) exhibit substantial advantages such as high integration, inherent signal amplification capability, low energy consumption, and ultrashort response times [26]. Caras and Janata [27] pioneered the innovative concept of combining FETs with enzymes, successfully immobilizing penicillinase on a FET with doped silicon as the channel material, achieving efficient detection of penicillin with an LOD of 0.2 mM, a response time of 25 s, and a sensing area of only 0.5 mm^2. Currently, commercially available detection platforms based on FETs are primarily used for continuous glucose monitoring, among other applications [28,29]. As applications and research progressed, the sensitivity of early FET biosensors became increasingly limited by their channel materials, such as silicon and tin oxide. Compared to 3-dimensional bulk channel materials, 2-dimensional (2D) materials represented by graphene (G) have an ultra-high specific surface area and ultra-thin thickness, which can serve as FET channel materials, achieving extremely high loading capacity and very low signal noise, leading to an extremely low theoretical LOD [7,30], among which the LOD for nucleic acid molecules is as low as 600 zM [31]. G FETs have demonstrated excellent performance in the detection of $A\beta_{42}$. In 2011, Cheng et al. [32] discovered that $A\beta_{42}$ could induce a substantial change in the channel current of G FETs, thereby proving the feasibility of using G FETs for the detection of $A\beta_{42}$. Subsequently, researchers confirmed that other materials (such as reduced graphene oxide [33] and carbon nanotubes [34,35]) could also serve as FET channel materials for detecting $A\beta_{42}$, with an LOD as low as 45 aM [35]. By virtue of surface functionalization [36] of the channel material or the use of aptamers [7,35,37] corresponding to $A\beta_{42}$ proteins as the target analyte, the limitations imposed by the material's inherent properties and the Debye length of the detection environment can be overcome. Up to now, femtomolar level of LOD of FET detection for $A\beta_{42}$ can be achieved by these strategies [33]; however, further improving sensitivity to meet clinical standards poses substantial challenges.

Here, we report a graphene–black phosphorus heterojunction (G-BP) FET optoelectronic biosensing platform for the precise and sensitive detection of AD biomarkers in blood. In the as-designed heterostructure, G serves as the channel material and BP, with its excellent photoresponse properties, serves as the photoactive layer. Under dark conditions, due to the high quality of the prepared G-BP FET and proper control of the Debye length, the $A\beta_{42}$ as a gate voltage signal increases the G channel current, thereby achieving effective detection of $A\beta_{42}$ with an LOD as low as 2.767×10^{-18} M (which is equivalent to 12.49 ag/ml or ~66.6 $A\beta_{42}$ molecules in 40 μl of detection solution). Under illumination, the same concentration of $A\beta_{42}$ not only increases the G channel current but also intensifies the band bending of BP. The photogenerated electron–hole pairs in BP are further separated compared to before the addition of $A\beta_{42}$, resulting in fewer photogenerated holes remaining in BP and a stronger photogating effect corresponding to the photogenerated electrons in BP, which further increases the G channel current. Therefore, the current change in the G-BP FET caused by the same concentration of $A\beta_{42}$ under illumination is markedly greater than that under dark conditions, which means that the LOD under illumination is much lower, reaching 2.351×10^{-19} M (which is equivalent to 1.061 ag/ml or ~5.7 $A\beta_{42}$ molecules in 40 μl of detection solution). Compared to the biosensing platforms reported so far, the LOD we achieved for the detection of $A\beta_{42}$ is the lowest, 2 to 3 orders of magnitude lower than other biosensing platforms. Due to the near-instantaneous nature of light triggering, the detection time under illumination is almost as short as that under dark conditions, approximately 5 min. With the help of this G-BP FET optoelectronic biosensing platform, ultra-sensitive detection of these AD biomarkers in blood can be achieved within several minutes. These results indicate that the light-triggered G-BP FET biosensor has great potential in early diagnosis and large-scale screening tests of AD.

Results and Discussion

Schematic diagram of the light-triggered G-BP FET biosensor

AD progression involves multiple biomarkers, such as $A\beta_{40}$, T-tau, P-tau, plasma neurofilament light chain, and plasma glial fibrillary acidic protein. Among these, $A\beta_{42}$ is one of the most extensively studied AD biomarkers due to its critical neurotoxic effects in synaptic degeneration. To validate the proof of concept of our light-triggered G-BP FET biosensing platform, we selected $A\beta_{42}$ as a representative target analyte to demonstrate its ultra-sensitive detection capability [38]. A schematic illustration of the $A\beta_{42}$ antigen protein is shown in Fig. 1A. The preparation method for $A\beta_{42}$, as well as $A\beta_{38}$ and $A\beta_{40}$ used in subsequent experiments, refers to our previous report [39]. The device structure is depicted in Fig. 1B, where G serves as the sensing channel of the device, and BP beneath the G absorbs light and generates a photogating effect to further amplify the sensing signal from the G. The detection process encompasses

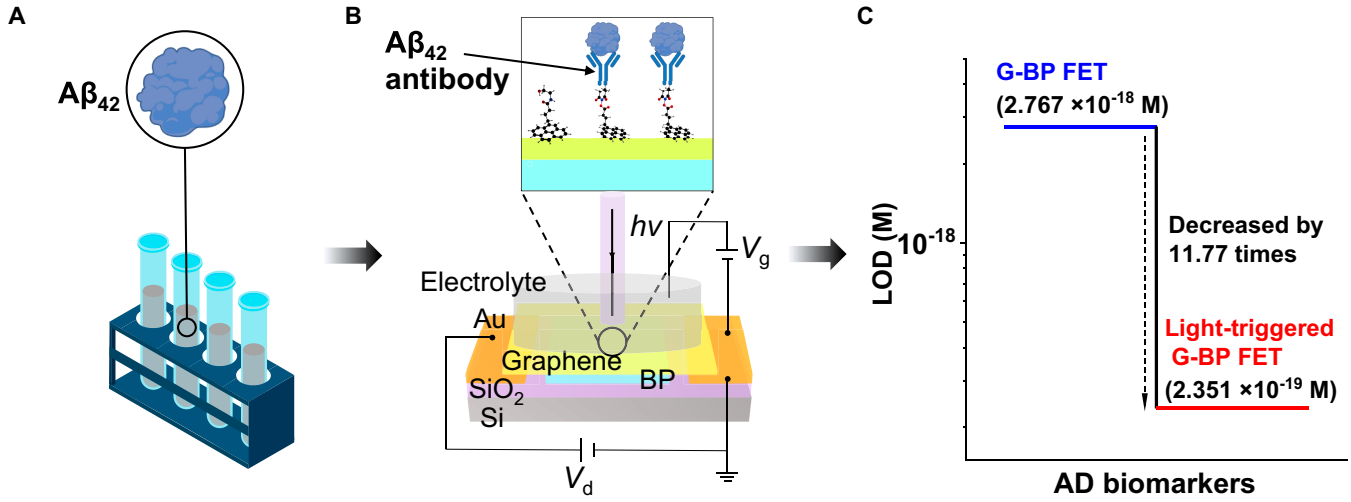


Fig. 1. Schematic diagram of G-BP FET biosensor operation procedure. (A) Schematic diagram of the $A\beta_{42}$ antigen. (B) Structural and principle diagram of light-triggered G-BP FET. (C) Effect of light on the detection of LOD of $A\beta_{42}$ protein by the G-BP FET biosensor. In the dark state, the LOD of the G-BP FET biosensor is 2.767 aM. In the light state, the LOD of the G-BP FET biosensor is 235.1 zM.

the modification of G surfaces with 1-pyrenebutyric acid N-hydroxysuccinimide ester (PBASE), the conjugation of $A\beta_{42}$ antibodies, the passivation of excess PBASE, and the collection of sensing current signals generated upon the specific binding of $A\beta_{42}$ antigenic proteins to $A\beta_{42}$ antibodies. Due to the high specificity of the $A\beta_{42}$ antibodies employed, G-BP FET modified with $A\beta_{42}$ antibodies exhibits superior detection performance. The LOD of the G-BP FET for $A\beta_{42}$ antigenic proteins is as low as 2.767×10^{-18} M, which is markedly lower than the results reported in other studies. More importantly, by subjecting the device to illumination, the signal current of the device is further amplified due to the grating effect of photogenerated electrons in BP, allowing the LOD of the G-BP FET to be reduced to 2.351×10^{-19} M (Fig. 1C).

Construction and characterization of biosensor

BP and G were used to prepare the G-BP heterojunction, and Raman spectroscopy showed that the G-BP heterojunction was successfully constructed (Fig. S1). The G-BP heterojunction is used as a channel material to fabricate FET devices (Figs. S2 and S3). In this system, G has 3 main functions. First, due to its high carrier mobility, G can act as a conductive channel [40]. Second, G's large specific surface area allows it to act as a sensing interface [41]. The modification of biomolecules on the G surface generates electrostatic gating that regulates channel conductivity, enabling efficient biomolecular recognition. Finally, G encapsulates BP, thereby isolating it from air and water and acting as a passivating agent [42]. As shown in Fig. S4, the Raman spectra of G-BP tested over 20 days of ambient exposure exhibited no variation in characteristic peaks, with stable peak intensities, strongly demonstrating the feasibility of G-encapsulated BP. BP has excellent optical properties and is used as a photosensitive material [43]. The G-BP FET biosensor platform developed in this study is shown in Fig. S5. FET is fixed to the chip carrier, far above the biosensing channel of polydimethylsiloxane (PDMS) used to contain the electrolyte solution and the liquid to be detected. Figure S6 depicts an optical image of a G-BP FET sensor with a sensing area size of $100 \times 40\ \mu m^2$ (L × W).

The functionalization of sensing surfaces is an important step in the construction of biosensors. Figure 2A illustrates in detail the process of functionalization of G-BP FET and detection of $A\beta_{42}$ protein. The PBASE, a commonly used and effective interfacial coupling agent, is utilized to immobilize $A\beta_{42}$ antibodies onto the G surface. The pyrene group at one end of PBASE is π–π stacked with G to form a self-assembled layer, which is uniformly modified on the surface of G [44]. The N-hydroxysuccinimide ester at the other end can react with the amine group on the modified $A\beta_{42}$ antibody through a primary amine reaction, allowing the antibody to be fixed on the sensing surface [45]. In order to verify the successful functionalization of PBASE, Raman spectroscopy and device electrical performance data were obtained. Figure 2B and C show the Raman spectra of different bands before and after modifying PBASE. The 3 characteristic peaks in Fig. 2B represent BP [46]. As shown in Fig. 2C, the peaks labeled *G* and *2D* are characteristic peaks of G [47]. The *G* peak is related to the lattice vibration mode, and the *2D* peak is derived from second-order Raman scattering. After modification with PBASE on the G surface, the characteristic peak exhibits a blue shift, indicating that the modification with PBASE has led to p-doping of the device, a doping effect resulting from the π–π interactions between PBASE and G [48]. Additionally, the average intensity ratio of the *2D* and *G* peaks (I_{2D}/I_G) serves as an indicator of the interaction between PBASE and G. Owing to the existence of some disorder on the G [45], the I_{2D}/I_G ratio of G modified with PBASE ($I_{2D}/I_G = 1.19$) was significantly lower than that of G unmodified with PBASE ($I_{2D}/I_G = 1.76$) [7].

In order to assess the degree of functionalization of the G surface, we performed electrical performance tests on the devices. Figure 2D shows the output characteristic curve in the range of −0.1 to +0.1 V during device functionalization. After functionalization of PBASE and fixation of $A\beta_{42}$ antibodies to the G surface, the slope of the curve gradually decreased (dI_d/dV_d), and this slope difference indicated the successful introduction of $A\beta_{42}$ antibodies. Subsequently, the transfer characteristic curves of G-BP FET devices after each modification process were tested (Fig. 2E). The G-BP FET device

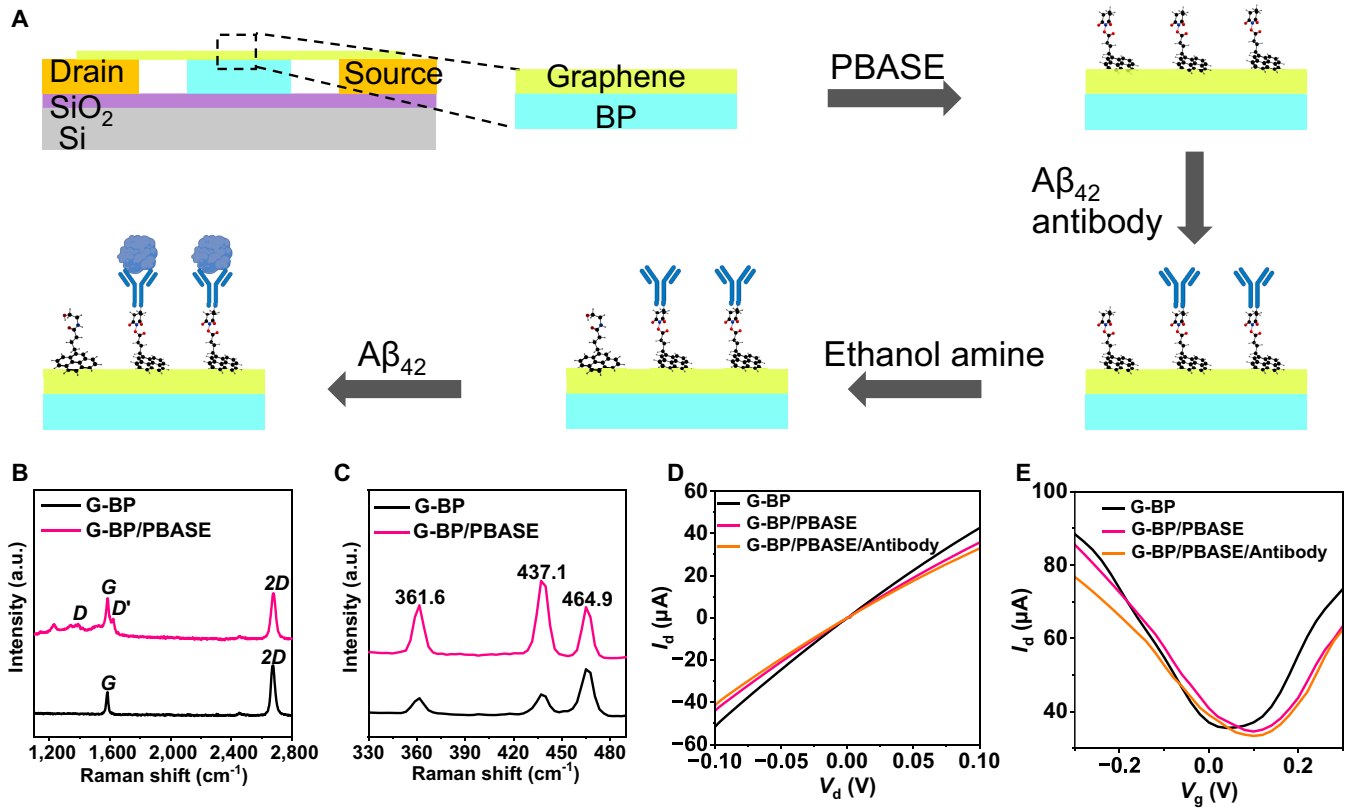


Fig. 2. Construction and characterization of the G-BP FET biosensor. (A) Schematic diagram of G-BP FET functionalization and detection of $A\beta_{42}$ protein. (B) Raman spectra (1,100 to 2,800 cm^{-1}) of G-BP before and after modification of PBASE. (C) Raman spectra (330 to 490 cm^{-1}) of G-BP before and after modification of PBASE. (D) Output characteristic curve of G-BP FET during functionalization (PBASE and antibody modifications). (E) Transfer characteristic curve of G-BP FET during functionalization ($V_d = 0.1$ V).

exhibits ambipolar characteristics with p-type dominance. After the modification of PBASE, a positive shift of the transfer characteristic curve was observed due to the p-doping effect of the pyrene group. Subsequently, the transfer curve after fixing the antibody was negatively shifted, which was due to the positive charge of the antibody in the detection environment, and the n-doping effect on the G. The change of output curve of the G-BP FET biosensor under different V_g values is shown in Fig. S7. V_g ranges from 0 to 0.4 V, and the step size is 0.1 V. When V_d is held constant, an increase in V_g leads to an increase in I_d, a phenomenon consistent with the expected characteristics of an n-type semiconductor. Furthermore, the linearity of the output characteristic curve indicates that the device has a highly stable ohmic contact, thereby suggesting that the G-BP FET biosensor provides a reliable electrical signal for the detection of $A\beta_{42}$ antigen.

Electrostatic photogating effect

Figure 3A is a schematic diagram of the detection process of $A\beta_{42}$ by the G-BP FET biosensing platform. Firstly, before the functionalization of the device, G forms a heterojunction with BP, inducing substantial changes in the energy band, as shown in Fig. 3B. The Fermi levels of G and BP before contact are approximately −4.85 and −4.7 eV, respectively [46]. Upon contact, the formation of a heterojunction between G and BP causes band bending in BP, resulting in the creation of an energy barrier. Figure 3 describes the principle of G-BP FET detection of $A\beta_{42}$ from the energy band perspective. The detection mechanism under dark conditions is shown in the middle of Fig. 3A. $A\beta_{42}$ is negatively charged in our detection solution (pH = 8.5) and physiological conditions [33]. When $A\beta_{42}$ (antigen) binds to the corresponding antibody on the device surface, the negatively charged $A\beta_{42}$ will exert an electrostatic gating effect on the G surface, in which an electric double layer (EDL) forms between $A\beta_{42}$ and the device surface [47–49], as shown in Fig. S8, leading to p-type doping of G, a decrease in the Fermi level by an amount $\Delta V_{A\beta42_dark}$, and consequently causing the G channel current to increase exponentially corresponding to $\Delta V_{A\beta42_dark}$ (see Section S1), as depicted in Fig. 3C. That is to say, even an extremely small amount of $A\beta_{42}$ can markedly increase the device's channel current through electrostatic gating, which supports the ultra-sensitive detection of $A\beta_{42}$, and subsequent experimental results show that under dark conditions, the LOD for $A\beta_{42}$ is as low as 2.767×10^{-18} M.

It is noteworthy that in FET biosensors, the gate control capability of the analyte over the channel is constrained by the screening effect of the test solution on the electric field, which substantially attenuates the biosensor signal [50]. Modeling of the screening effect typically relies on a simple capacitive model based on the linearized Poisson–Boltzmann equation, which is used to describe the distribution of potential attenuation in the presence of mobile charges. The Debye length stems from this concept, characterizing the spatial scale of potential decay as a characteristic value, providing a useful standard for the spatial scale of electric field screening [50]. Under physiological conditions, the Debye length is less than 1 nm, whereas most antibodies are about 10 to 15 nm in length. In our previous research, the length of the $A\beta_{42}$ antibody was measured to be approximately 64.9 nm [2,50], indicating that the ideal Debye

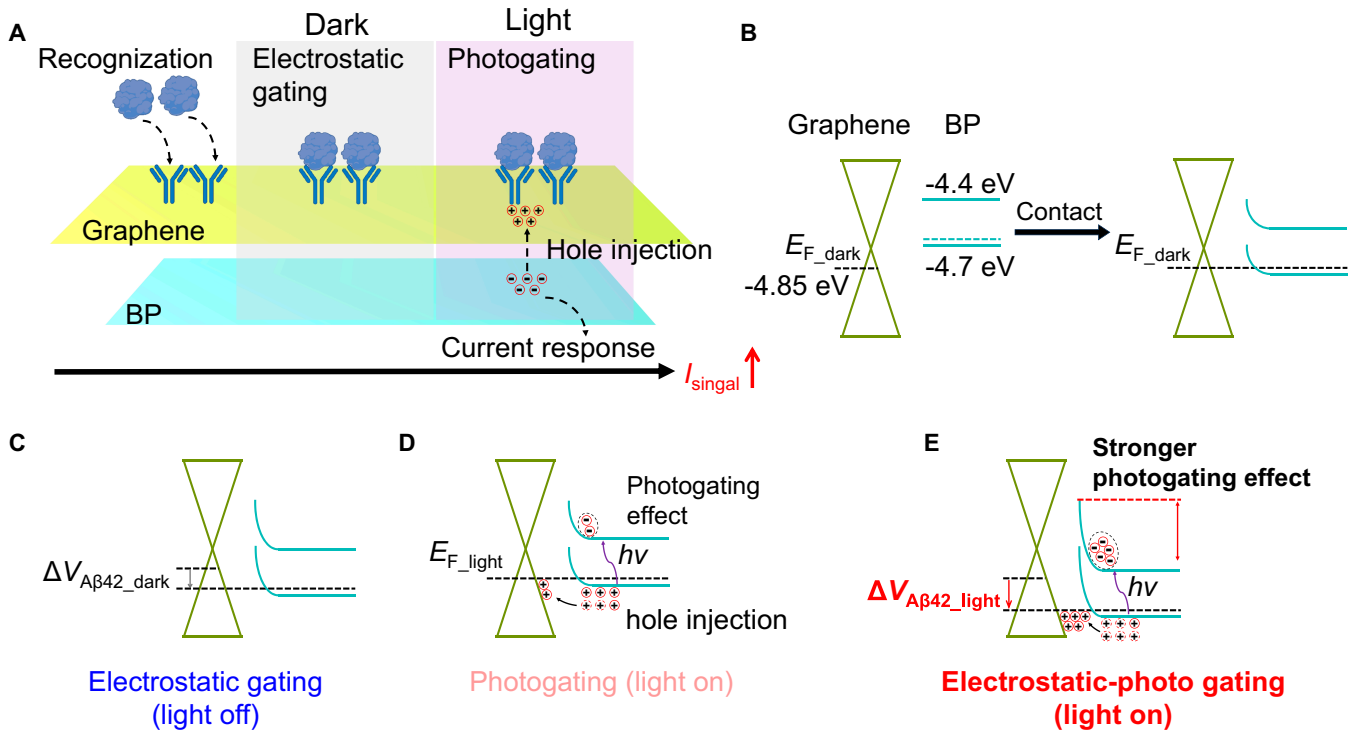


Fig. 3. Mechanism of electrostatic photogating. (A) Schematic illustration of $A\beta_{42}$ protein detection by G-BP FET using the electrostatic photogating mechanism. (B) Energy band changes before and after the formation of heterojunction between G and BP. (C) Energy band variation diagram of G-BP in the electrostatic gating process. (D) Energy band variation diagram of G-BP in the photogating process. (E) Energy band variation diagram of G-BP in the electrostatic photogating process.

length in our detection environment needs to be greater than 64.9 nm. Therefore, we increased the Debye length from the physiological level of 1 to ~23 nm by using a low-concentration buffer (0.001× phosphate-buffered saline [PBS]) [51]. Our experimental results indicate that the G-BP FET can already achieve sensitive detection of $A\beta_{42}$ in a 0.001× PBS buffer solution, which seems to be inconsistent with the aforementioned Debye length requirement. We suspect that this anomalous phenomenon may arise from 2 factors: (a) Some $A\beta_{42}$ specifically binding to the antibody surface in a non-perpendicular orientation, which may make the distance between $A\beta_{42}$ and the G surface smaller than the original Debye length; and (b) the reduced Debye volume (the available volume of EDL) caused by surface indentation of G induced by the underlying thicker BP layer and localized wrinkles generated during the G transfer process. The reduction in Debye volume enables the G-BP FET to be used for $A\beta_{42}$ detection beyond the Debye length.

The photon energy of the light source is approximately 2.33 eV, exceeding the bandgaps of BP (0.3 eV) and G (0 eV). When photons irradiate the device, valence band electrons in black phosphorus or graphene absorb photon energy and transition to the conduction band, generating photogenerated carriers. When BP was exposed to photons with energy equal to or greater than its bandgap, electrons in the valence band are excited into the conduction band, leaving behind holes. These holes are driven into the G by the built-in electric field, while the photoexcited electrons are trapped in the energy barrier at the BP interface. The accumulated photoexcited electrons act as a local gate, p-doping the G channel, as shown in Fig. 3D, thereby increasing the G channel current. As shown in Fig. S9, the channel current of the pristine G FET hardly changes under illumination, indicating that compared to the G-BP FET, the pristine G FET has a negligible photoresponse. The detection mechanism under light illumination is shown on the right side of Fig. 3A. When $A\beta_{42}$ was added to the detection solution under light illumination, it first causes the G channel current to increase to the same extent as when the same concentration of $A\beta_{42}$ was added in the dark (the Fermi level is lowered by the same degree). This further intensifies the band bending of BP, and the photogenerated electron–hole pairs in BP are more separated than before the addition of the $A\beta_{42}$. The reduction of photogenerated holes remaining in BP leads to a stronger photogating effect corresponding to the photogenerated electrons, which will further increase the G channel current (further lower the Fermi level). Therefore, the change in G-BP FET current caused by the same concentration of $A\beta_{42}$ under illumination (the total change in Fermi level is denoted as $\Delta V_{A\beta42_light}$) is markedly greater than that under dark conditions, as illustrated in Fig. 3E. This conclusion can also be drawn from the transfer curves in Fig. S10. Specifically, in the dark state, after the addition of 100 pM $A\beta_{42}$ to the G-BP FET detection platform, the ΔV_{Dirac} in the transfer curve is 5 mV, and this value markedly increases to 20 mV under illumination. Furthermore, under illumination, the response of the pristine G FET to 100 pM $A\beta_{42}$ is approximately 11.00% (Fig. S11), while the response of the G-BP FET is substantially higher, at 47.70% (Fig. 4D). Based on the analysis above, under illumination, a much lower LOD is achieved, reaching 2.351×10^{-19} M.

Detection of $A\beta_{42}$ protein by light-triggered G-BP FET biosensor

As illustrated in the schematic diagram of the biosensor in Fig. 4A, the G-BP FET biosensor can detect $A\beta_{42}$ by monitoring the changes in surface charge on the channel and channel current.

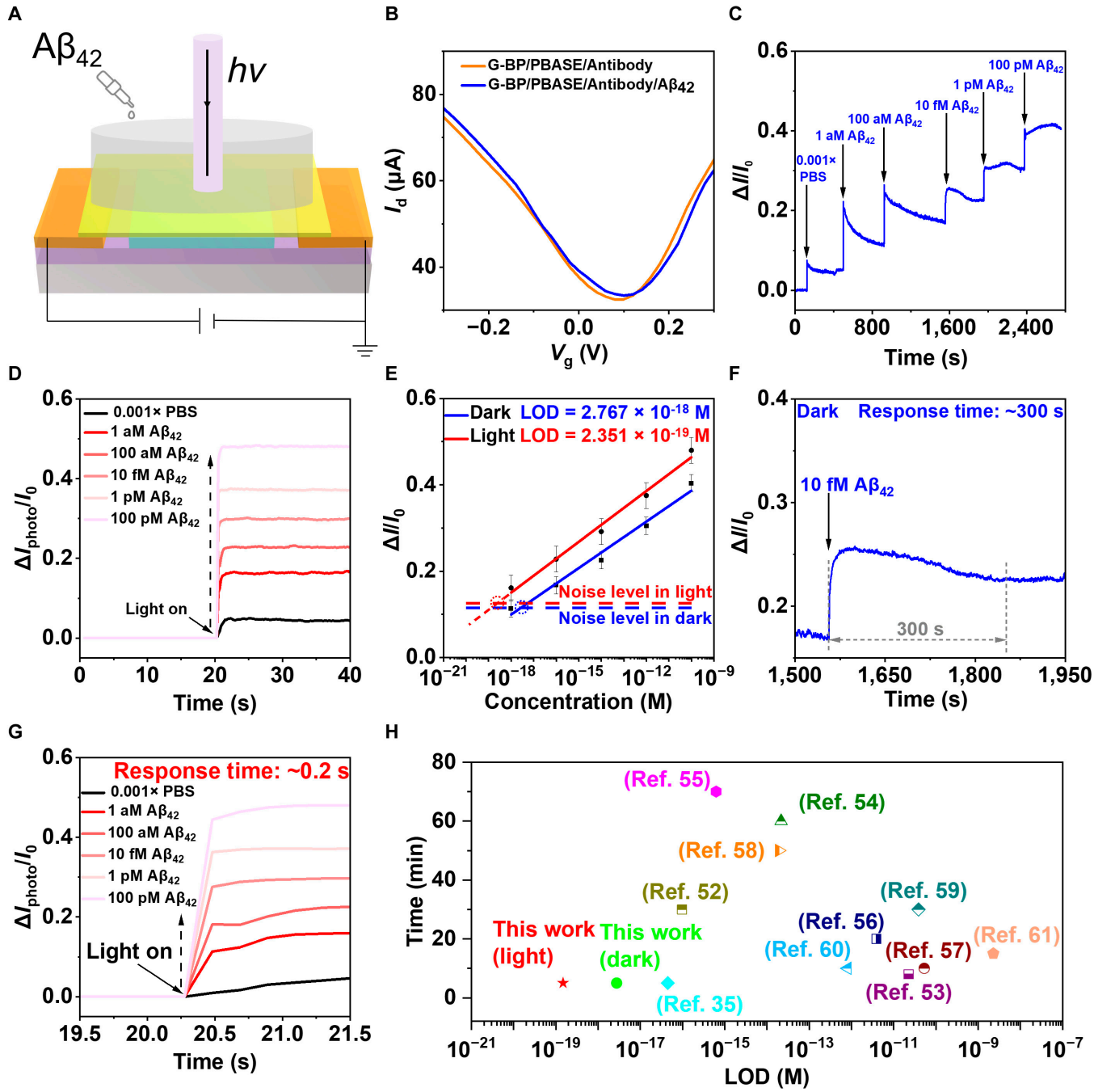


Fig. 4. $A\beta_{42}$ biomarker detection. (A) Schematic diagram of detecting $A\beta_{42}$ by G-BP FET. (B) The transfer characteristic curve of $A\beta_{42}$ was detected by G-BP FET ($V_d = 0.1$ V). (C) Real-time response of G-BP FET to $A\beta_{42}$ in 0.001× PBS in the dark state. (D) The response curve of the G-BP FET biosensor changed with time after adding $A\beta_{42}$ with a concentration of 0 to 100 pM to 0.001× PBS. From 20 s onwards, the device is exposed to light. (E) Relationship between $A\beta_{42}$ concentration and response signal. The intersection of noise level and curve is LOD. LOD is 2.767 aM in the dark and 235.1 zM in the light. (F) The response time of 10 fM $A\beta_{42}$ was detected in the dark state. (G) Light response time of the G-BP FET sensor under different $A\beta_{42}$ concentrations. (H) The performance of this work was compared with other methods for the detection of $A\beta_{42}$.

Figure 4B describes the changes of the device's transfer curves before and after adding $A\beta_{42}$. The specific binding between $A\beta_{42}$ and the corresponding antibody (1F12) caused a positive shift in the transfer curve, indicating that $A\beta_{42}$ introduced a p-doping effect on G.

To evaluate the effectiveness of the G-BP FET biosensor, we meticulously assessed the sensor's real-time response to $A\beta_{42}$. We defined a parameter ($\Delta I / I_0$) to represent the change in signal, expressed as:

$$\Delta I / I_0 = \frac{I - I_0}{I_0} \quad (1)$$

where I_0 and I represent the channel current of the biosensor before and after the introduction of $A\beta_{42}$, respectively.

As shown in Fig. 4C, the response of the biosensor markedly increases with the increasing of concentration of $A\beta_{42}$. The $\Delta I / I_0$ response at $A\beta_{42}$ concentrations of 1 aM and 100 pM is ~11.37% and ~40.10%, respectively. These experimental

phenomena confirm that the G-BP FET biosensor exhibits high sensing capabilities for $A\beta_{42}$ under dark conditions. Next, we investigated the impact of light on the detection process. Under illumination of 12.7 mW/cm^2, the detection data for $A\beta_{42}$ by the G-BP FET biosensor is shown in Fig. 4D. The results indicate that $A\beta_{42}$ can also be detected under light conditions, with the response signal being positively correlated with the concentration of $A\beta_{42}$, a trend that is consistent with the dark state. It is worth noting that the biosensor's response to 100 pM $A\beta_{42}$ is 48.00% and 40.10% under illumination and dark, indicating that light triggering can enhance the biosensing signal.

Additionally, we explored the correlation between the concentration of $A\beta_{42}$ and the response of $\Delta I / I_0$. The error bars were obtained from 3 repeated experiments. Under both conditions, the response of $\Delta I / I_0$ showed a linear relationship with the logarithm of the $A\beta_{42}$ concentration (Fig. 4E), and the linear fits are given by:

$$\Delta I_{\text{dark}} / I_0 = 0.03588 \log C + 0.74527 \quad (2)$$

$$\Delta I_{\text{light}} / I_0 = 0.03920 \log C + 0.85605 \quad (3)$$

We have thoroughly discussed the origin of the linear relationship between $\Delta I / I_0$ and $A\beta_{42}$ in Section S1. The data indicate that the G-BP FET biosensor exhibits higher sensitivity under illumination (slope = 0.03920) than under dark

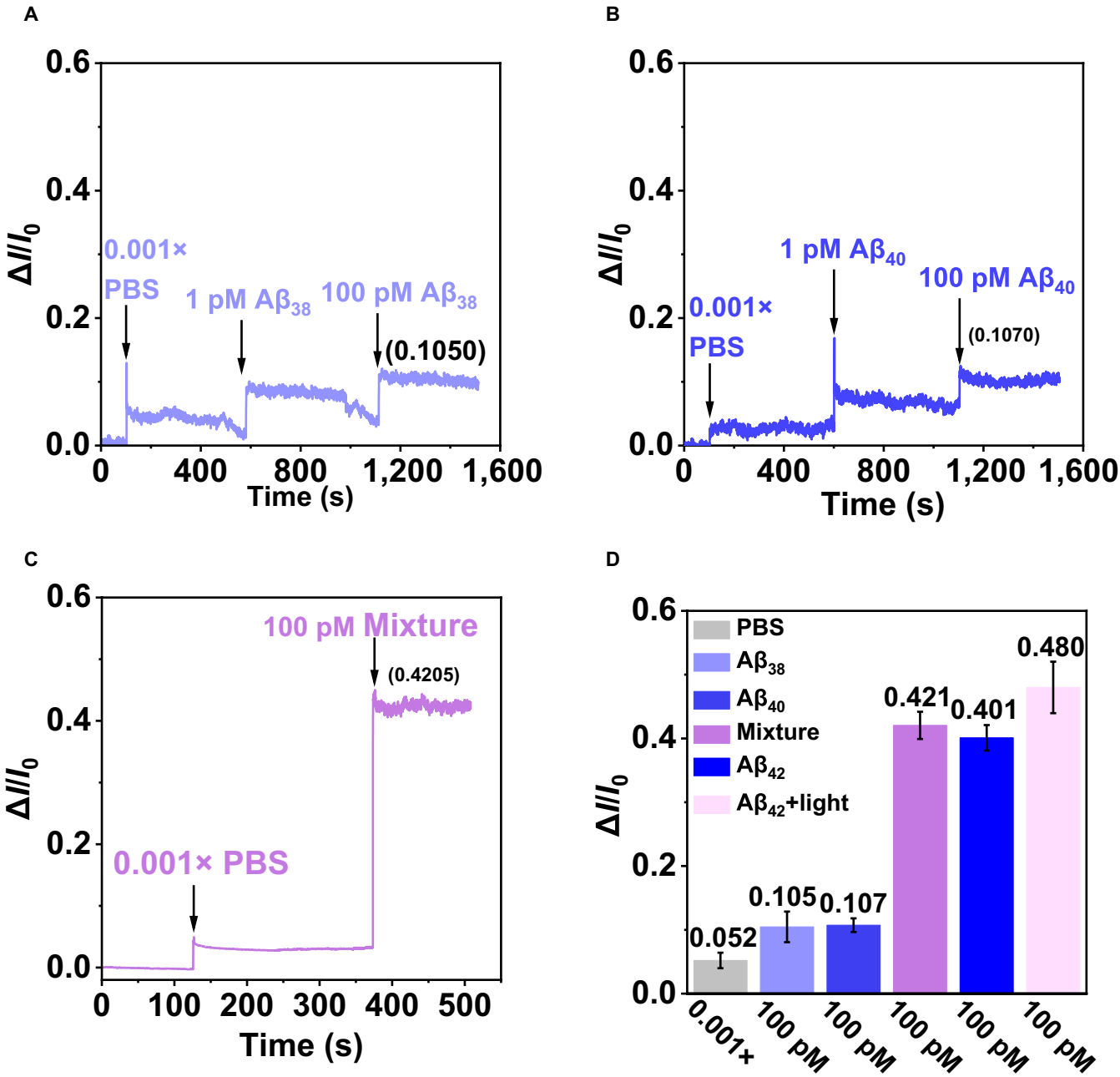


Fig. 5. Specificity verification of the G-BP FET biosensor. (A) Real-time response of G-BP FET to $A\beta_{38}$ in 0.001× PBS. (B) Real-time response of G-BP FET to $A\beta_{40}$ in 0.001× PBS. (C) Real-time response of G-BP FET to mixed peptides in 0.001× PBS. (D) Response signals of PBS (0.001×), $A\beta_{38}$ (100 pM), $A\beta_{40}$ (100 pM), mixed peptides (100 pM), and $A\beta_{42}$ (100 pM and 100 pM + light).

(slope = 0.03588). Additionally, the LOD can be determined by the intersection of the noise level with the fitting curve (as detailed in Section S2). The results show that the LOD under illumination (235.1 zM) is 11.77 times lower than the LOD under dark (2.767 aM).

The response time is ~300 s under dark, as shown in Fig. 4F extracted from Fig. 4C. Under illumination, the time required for the response signal caused by the photogating effect is only ~0.2 s, as shown in Fig. 4G extracted from Fig. 4D. Therefore, when the G-BP FET is used for detection under illumination, the detection time is ~300.2 s, indicating that the light-triggered G-BP FET almost maintains the fast response characteristic of the G-BP FET used for biosensing.

Furthermore, stability is one of the key indicators for evaluating the sensing performance of the G-BP FET. Therefore, a series of repeatable responses spanning 9 on–off cycles were performed for the G-BP FET sensing platform over a continuous duration of 400 s, with results shown in Fig. S12. The current variation remained largely consistent throughout the 9 light-switching cycles, demonstrating the excellent stability of the system. Next, the optical response performance of 100 pM $A\beta_{42}$ was detected on the 1st and 20th days, respectively, using the same G-BP FET device. The results, as shown in Fig. S13, indicate that the average photocurrent response amplitude remains at 86.04% of the initial value.

We compared with other reported methods from the perspective of LOD and response time [39], as shown in Fig. 4H. The LOD of the light-triggered G-BP FET is about 3 orders of magnitude lower than traditional techniques such as surface-enhanced Raman scattering spectroscopy [14], FET sensors [35,52], electrochemical sensors [53,54], electrochemical immunoluminescence analysis [55], molecular imprinting sensors [56], and other traditional measurement methods [57–61]. Furthermore, the response time of the G-BP FET for biosensing is almost record short.

We investigated the specificity of the G-BP FET biosensor. $A\beta_{38}$ and $A\beta_{40}$ were introduced for detection under dark, and the results showed that the $\Delta I / I_0$ response of the G-BP FET to 100 pM $A\beta_{38}$ and 100 pM $A\beta_{40}$ were 10.50% and 10.70%, respectively (Fig. 5A and B). Both of these values are lower than the noise caused by pure 0.001× PBS (11.529%), indicating that $A\beta_{38}$ and $A\beta_{40}$ could not be detected. The weak signals exhibited here can be attributed to the non-specific adsorption of $A\beta_{38}$ and $A\beta_{40}$ on the sensing interface. Next, we evaluated the response of the G-BP FET biosensing platform to a mixed peptide solution (containing 100 pM $A\beta_{38}$, $A\beta_{40}$, and $A\beta_{42}$) under dark conditions. As shown in Fig. 5C, the mixed peptides elicited a response signal of approximately 42.10%, demonstrating the platform's capability to selectively detect $A\beta_{42}$ in complex matrix environments despite the presence of structurally similar Aβ isoforms. Figure 5D summarizes the changes in channel current caused by $A\beta_{38}$, $A\beta_{40}$, and $A\beta_{42}$ at different concentrations, and it can be seen that the G-BP FET responds strongly only to $A\beta_{42}$, while illumination further enhances the response signal, demonstrating the high specificity of the G-BP FET biosensor for $A\beta_{42}$.

To validate the performance of the light-triggered G-BP FET biosensing platform in complex solution environments, the detection capability of the G-BP FET for $A\beta_{42}$ in serum environments was tested. As shown in Fig. S14, the G-BP FET exhibited clear response signals to $A\beta_{42}$ at varying concentrations under both dark and illuminated states, with the response signals increasing markedly as $A\beta_{42}$ concentration rose. This strongly demonstrates the feasibility of the light-triggered G-BP FET biosensor for $A\beta_{42}$ detection in serum environments. By fitting the relationship between response signals and concentrations, a linear fitting function was derived:

$$\Delta I_{\text{dark}} / I_0 = 0.05346 \log C + 1.05967 \quad (4)$$

$$\Delta I_{\text{light}} / I_0 = 0.05500 \log C + 1.12787 \quad (5)$$

Finally, the LOD for $A\beta_{42}$ in serum was calculated, yielding values of 4.440 aM in the dark state and 1.932 aM under illumination.

In addition, the reliance of the G-BP FET sensor on antibodies for target capture introduces inherent limitations to its detection performance, as the sensor's sensitivity and stability remain constrained by antibody-dependent factors such as binding affinity and degradation resistance, highlighting a current drawback of the platform.

Conclusion

In summary, we report a light-triggered G-BP FET biosensing platform for precise, sensitive, and fast detection of AD blood-oriented biomarkers. In the as-designed heterojunction, G serves as the channel material, and BP, with its excellent photo responsive performance, acts as the photo driven layer. Under dark, thanks to the high quality of the prepared G-BP FET devices and proper control of the Debye length, effective detection of $A\beta_{42}$ was achieved, with an LOD as low as 2.767×10^{-18} M. Under illumination, due to the photogating effect, a much lower LOD was achieved, reaching 1.491×10^{-19} M. Among the biosensing platforms reported to date, the LOD we achieved for the detection of $A\beta_{42}$ is the lowest, 3 orders of magnitude lower than other biosensing platforms. The detection time of the light-triggered G-BP FET is ~300.2 s. With the help of this G-BP FET photoelectric sensing platform, ultra-sensitive detection of the AD blood-oriented biomarkers can be achieved within several minutes. These results indicate that the light-triggered G-BP FET biosensor has great potential in the early diagnosis and large-scale screening tests of AD.

Materials and Methods

Materials

G was purchased from Nanjing Muke Nanotechnology Co., Ltd. (Nanjing, China). BP was purchased from Nanjing XFNANO Materials Tech Co., Ltd. (Nanjing, China). $A\beta_{38}$, $A\beta_{40}$, and $A\beta_{42}$ were custom-synthesized as lyophilized powders by Royo Biotech Co., Ltd (Shanghai, China) with a purity of >95%. PBASE was acquired from Thermo Fisher Scientific (Waltham, MA).

Preparation of few-layer black phosphorus

In this study, a mechanical stripping technique was employed to prepare a few-layer BP. First, take a 10-cm-long piece of transparent tape and repeatedly place bulk BP in the middle of the transparent tape, leaving an appropriate amount of BP. Second, fold the tape about 100 times to ensure that the BP is evenly distributed throughout the tape. Then, cut a piece of PDMS film with a size of about 0.5 × 0.5 cm^2, remove 2 layers of protective film, paste it on a clean glass sheet, paste the folded tape on the PDMS film, apply firm pressure within the specified time, and remove the tape in time. Finally, a thin layer of BP is transferred to the PDMS film, and a small amount of BP layers

on the PDMS film are observed using an optical microscope, and a suitable layer is selected for subsequent transfer.

Preparation of single layer graphene

Monolayer G was obtained by etching copper-based PMMA/G. First, prepare the etching solution. The etching solution consisted of a mixture of 40 ml of 30 g/l hydrogen peroxide and 4 ml of 36% hydrochloric acid. Secondly, cut a piece of copper-based PMMA/G sized approximately 0.25×0.25 cm^2, and immerse it in the etching solution. The etching process was conducted for approximately 10 min. Finally, once the PMMA/G became completely transparent, transfer the clean slide to deionized water for 10 min and repeat the washing process 3 times.

Fabrication of devices

Initially, transfer the few-layer BP from the PDMS film to the channel of the SiO_2/Si substrate. Attach the cleaned silicon wafer to the PDMS film, apply gentle pressure, heat to 80 °C, and maintain a constant temperature for 10 min prior to separation. At this stage, a small layer of BP has been successfully transferred to a specific location on the silicon chip. Subsequently, use a silicon wafer with transferred few-layer BP to quickly scoop up the PMMA/G in the deionized water. Then, quickly rinse in isopropyl alcohol. Next, wash the device in acetone for 1 min to eliminate PMMA from the G surface. Lastly, rinse the device 3 times with isopropyl alcohol and dry with nitrogen. Dry the prepared devices overnight under vacuum conditions.

Functionalization of graphene surface

The prepared devices were soaked in a 5 mM PBASE solution in methanol for 30 min at room temperature, subsequently washed 3 times with 10 μM PBS buffer and deionized water, and then incubated in a 1 μM $A\beta_{42}$ antibody [2,62] solution for 4 h (Fig. S15).

Characterization

The preparation and functionalization of the materials were characterized by Raman spectroscopy. Raman scattering analysis was conducted using the alpha300 R confocal Raman imaging microscope system (Oxford Instruments WITec). This microscope is equipped with a 532-nm laser serving as the excitation source.

Device measurement

As a biosensor, PDMS well is positioned above the channel to contain a 40-μl analyte solution, with the gate probe of the probe station serving as the liquid gate electrode. Electrical measurements are conducted at room temperature using a semiconductor analyzer (Keithley Instruments, 4200-SCS). When $V_g = 0$ V, the I_d–V_d output curve is obtained by scanning the I_d for V_d ranging from −1 to 1 V. At $V_d = 0.1$ V, the I_d–V_g transfer curve is obtained by scanning the V_g within the range of −1 to 1 V, and the Dirac point is determined at the juncture where I_d reaches its minimum value. In the photocurrent test, utilize an optical chopper (OEABT, OBS-C1) to control the ON–OFF state of lighting, with measurements of the light-triggered chemo-transistor conducted in a dark sealed box. The light source is provided by the 532-nm laser.

Detection of $A\beta_{42}$ protein

The detection of $A\beta_{42}$ was assessed using a semiconductor analyzer and a probe station. The molecular weight of $A\beta_{42}$ used in this work is 4,514.03 g/mol. During measurements in 10 μM PBS, a stable bias ($V_d = 0.1$V) is applied between the drain and source. Once the I_d was stabilized, varying concentrations of $A\beta_{42}$ were introduced for testing. The electrical response signal detected is normalized to $\Delta I/I_0$.

Acknowledgments

We thank the Photonics Center of Shenzhen University for technical support and the support from the Instrumental Analysis Center of Shenzhen University (Xili Campus).

Funding: H.W. acknowledges funding from the National Natural Science Foundation of China (62405195). H.W. and N.F. acknowledge funding from Shenzhen Science and Technology Program (KCXFZ20230731093359004). M.Q. acknowledges funding from the National Natural Science Foundation of China (62375249), the Taishan Scholar Project (tsqn201909054), and the Natural Science Foundation of Shandong Province (ZR2022JQ22). Q.L. acknowledges funding from the STI2030-Major Projects (grant no. 2021ZD0201001) and the Chinese Academy of Medical Sciences (CAMS) Innovation Fund for Medical Sciences (grant no. 2019-I2M-5-014). H.L. acknowledges funding from the National Natural Science Foundation of China (grant no. 81971025). H.Z. acknowledges funding from the State Key Research Development Program of China (grant no. YS2022YFB3200011), LingChuang Research Project of China National Nuclear Corporation (no. CNNC-LCKY-202268), the Department of Education of Guangdong Province (no. 2022ZDZX1023), the Basic and Applied Basic Research Foundation of Guangdong Province-Regional Joint Fund-Key Projects (2022B1515120012), the Central Military Commission Science and Technology Committee Project (2022-JCJQ-JJ-0886), the Science and Technology Innovation Commission of Shenzhen (KCXFZ20211020163814021), Key Projects (B) of the Stability Support Program for Shenzhen Higher Education Institutions (no. 20220810151419001), the Research Team Cultivation Program of ShenZhen University (grant no. 2023QNT008), the Hangzhou Normal University "Project to the summit" chemical discipline, the Ministry of Education Key Laboratory Open Scientific Projects Fund (KFJJ2023007), and a project supported by State Key Laboratory of Luminescence and Applications(SKLA-2020-03).

Author contributions: Conceptualization: H.W., M.Q., C.W., L.Z., H.L., and H.Z. Methodology: H.W., M.Q., C.W., L.Z., Z.C., Y.L., T.L., Z.W., Y. Zhu, Y. Zhang, X.T., Y.W., M.Y., D.F., K.J., H.L., and H.Z. Data analysis: H.W., M.Q., C.W., H.L., and H.Z. Resources: H.W., M.Q., Q.L., H.L., and H.Z. Writing—original draft: H.W., M.Q., and C.W. Writing—review and editing: H.W., M.Q., C.W., H.L., and H.Z. Funding acquisition: H.W., M.Q., N.F., Q.L., H.L., and H.Z.

Competing interests: The authors declare that they have no competing interests.

Data Availability

All data relevant to this study are available in the manuscript and supporting information. Raw data are available from the corresponding authors upon reasonable request.

Supplementary Materials

Supplementary Text
Figs. S1 to S15
References [63–68]

References

1. Scheltens P, De Strooper B, Kivipelto M, Holstege H, Chetelat G, Teunissen CE, Cummings J, van der Flier WM. Alzheimer's disease. *Lancet*. 2021;397(10284):1577–1590.
2. Zhang L, Du X, Su Y, Niu S, Li Y, Liang X, Luo H. Quantitative assessment of ad markers using naked eyes: Point-of-care testing with paper-based lateral flow immunoassay. *J Nanobiotechnol*. 2021;19(1):366.
3. Armstrong RA. The pathogenesis of Alzheimer's disease: A reevaluation of the "amyloid cascade hypothesis". *Int J Alzheimers Dis*. 2011;2011(1):630865.
4. Khachaturian ZS. Diagnosis of Alzheimer's disease. *Arch Neurol*. 1985;42(11):1097–1105.
5. Mirra SS, Heyman A, McKeel D, Sumi S, Crain BJ, Brownlee L, Vogel F, Hughes J, van Belle G, Berg L. The Consortium to Establish a Registry for Alzheimer's disease (Cerad). Part II. Standardization of the neuropathologic assessment of Alzheimer's disease. *Neurology*. 1991;41(4):479–479.
6. Newell KL, Hyman BT, Growdon JH, Hedley-Whyte ET. Application of the National Institute on Aging (NIA)-Reagan institute criteria for the neuropathological diagnosis of Alzheimer disease. *J Neuro-Oncol*. 1999;58(11):1147–1155.
7. Bodily TA, Ramanathan A, Wei S, Karkisaval A, Bhatt N, Jerez C, Haque MA, Ramil A, Heda P, Wang Y, et al. In pursuit of degenerative brain disease diagnosis: Dementia biomarkers detected by DNA aptamer-attached portable graphene biosensor. *Proc Natl Acad Sci USA*. 2023;120(47): Article e2311565120.
8. Hu S, Yang C, Luo H. Current trends in blood biomarker detection and imaging for Alzheimer's disease. *Biosens Bioelectron*. 2022;210:114278.
9. Hu S, Zhang L, Su Y, Liang X, Yang J, Luo Q, Luo H. Sensitive detection of multiple blood biomarkers via immunomagnetic exosomal PCR for the diagnosis of Alzheimer's disease. *Sci Adv*. 2024;10(13):Article eabm3088.
10. Stenh C, Englund H, Lord A, Johansson AS, Almeida CG, Gellerfors P, Greengard P, Gouras GK, Lannfelt L, Nilsson LN. Amyloid-B oligomers are inefficiently measured by enzyme-linked immunosorbent assay. *Ann Neurol*. 2005;58(1):147–150.
11. Yang T, Hong S, O'Malley T, Sperling RA, Walsh DM, Selkoe D. New ELISAs with high specificity for soluble oligomers of amyloid B-protein detect natural aβ oligomers in human brain but not CSF. *Alzheimers Dement*. 2013;9(2): 99–112.
12. Li H, Xie H, Cao Y, Ding X, Yin Y, Li G. A general way to assay protein by coupling peptide with signal reporter via supermolecule formation. *Anal Chem*. 2013;85(2):1047–1052.
13. Guerrini L, Arenal R, Mannini B, Chiti F, Pini R, Matteini P, Alvarez-Puebla RA. Sers detection of amyloid oligomers on metallorganic-decorated plasmonic beads. *ACS Appl Mater Interfaces*. 2015;7(18):9420–9428.
14. Zhu W, Wang Y, Xie D, Cheng L, Wang P, Zeng Q, Li M, Zhao Y. In situ monitoring the aggregation dynamics of amyloid-B protein Aβ42 in physiological media via a Raman-based frequency shift method. *ACS Appl Bio Mater*. 2018;1(3):814–824.
15. Zhu L, Zhang J, Wang F, Wang Y, Lu L, Feng C, Xu Z, Zhang W. Selective amyloid B oligomer assay based on abasic site-containing molecular beacon and enzyme-free amplification. *Biosens Bioelectron*. 2016;78:206–212.
16. Rushworth JV, Ahmed A, Griffiths HH, Pollock NM, Hooper NM, Millner PA. A label-free electrical impedimetric biosensor for the specific detection of Alzheimer's amyloid-beta oligomers. *Biosens Bioelectron*. 2014;56:83–90.
17. Veloso AJ, Chow AM, Ganesh HV, Li N, Dhar D, Wu DC, Mikhaylichenko S, Brown IR, Kerman K. Electrochemical immunosensors for effective evaluation of amyloid-beta modulators on oligomeric and fibrillar aggregation processes. *Anal Chem*. 2014;86(10):4901–4909.
18. Xia N, Wang X, Zhou B, Wu Y, Mao W, Liu L. Electrochemical detection of amyloid-B oligomers based on the signal amplification of a network of silver nanoparticles. *ACS Appl Mater Interfaces*. 2016;8(30):19303–19311.
19. Zhang L, Cao K, Su Y, Hu S, Liang X, Luo Q, Luo H. Colorimetric and surface-enhanced Raman scattering dual-mode magnetic immunosensor for ultrasensitive detection of blood phosphorylated tau in Alzheimer's disease. *Biosens Bioelectron*. 2023;222:114935.
20. Zhang L, Su Y, Liang X, Cao K, Luo Q, Luo H. Ultrasensitive and point-of-care detection of plasma phosphorylated tau in Alzheimer's disease using colorimetric and surface-enhanced Raman scattering dual-readout lateral flow assay. *Nano Res*. 2023;16(5):7459–7469.
21. Hansson O, Edelmayer RM, Boxer AL, Carrillo MC, Mielke MM, Rabinovici GD, Salloway S, Sperling R, Zetterberg H, Teunissen CE, et al. The Alzheimer's Association appropriate use recommendations for blood biomarkers in Alzheimer's disease. *Alzheimers Dement*. 2022;18(12):2669–2686.
22. Hansson O, Blennow K, Zetterberg H, Dage J. Blood biomarkers for Alzheimer's disease in clinical practice and trials. *Nat Aging*. 2023;3(5):506–519.
23. Jack CR Jr, Andrews SJ, Beach TG, Buracchio T, Dunn B, Graf A, Hansson O, Ho C, Jagust W, McDade E. Revised criteria for the diagnosis and staging of Alzheimer's disease. *Nat Med*. 2024;30(8):2121–2124.
24. Zhou J, Benoit M, Sharoar MG. Recent advances in pre-clinical diagnosis of Alzheimer's disease. *Metab Brain Dis*. 2022;37(6):1703–1725.
25. Yan Y, Wang C. AB_{40} protects non-toxic $A\beta_{42}$ monomer from Aggregation. *J Mol Biol*. 2007;369(4):909–916.
26. Zhuo F, Wu J, Li B, Li M, Tan CL, Luo Z, Sun H, Xu Y, Yu Z. Modifying the power and performance of 2-dimensional MoS_2 field effect transistors. *Research*. 2023;6:0057.
27. Caras S, Janata J. Field effect transistor sensitive to penicillin. *Anal Chem*. 1980;52(12):1935–1937.
28. Hovorka R. Continuous glucose monitoring and closed-loop systems. *Diabet Med*. 2006;23(1):1–12.
29. Shichiri M, Yamasaki Y, Kawamori R, Hakui N, Abe H. Wearable artificial endocrine pancreas with needle-type glucose sensor. *Lancet*. 1982;320(8308):1129–1131.
30. Wang L, Xu C, Zhang S, Chen S, Wang H, Duan Z, Al-Hartomy OA, Wageh S, Wen X, Liu Y. Rapid and ultrasensitive detection of mpox virus using CRISPR/Cas12b-empowered graphene field-effect transistors. *Appl Phys Rev*. 2023;10(3):031409.
31. Hwang MT, Heiranian M, Kim Y, You S, Leem J, Taqieddin A, Faramarzi V, Jing Y, Park I, van der Zande AM, et al. Ultrasensitive detection of nucleic acids using deformed graphene channel field effect biosensors. *Nat Commun*. 2020;11(1):1543.
32. Cheng Z, Zhou Q, Wang C, Li Q, Wang C, Fang Y. Toward intrinsic graphene surfaces: A systematic study on thermal annealing and wet-chemical treatment of SiO_2-supported graphene devices. *Nano Lett*. 2011;11(2):767–771.

33. Park D, Kim JH, Kim HJ, Lee D, Lee DS, Yoon DS, Hwang KS. Multiplexed femtomolar detection of Alzheimer's disease biomarkers in biofluids using a reduced graphene oxide field-effect transistor. *Biosens Bioelectron*. 2020;167:112505.
34. Oh J, Yoo G, Chang YW, Kim HJ, Jose J, Kim E, Pyun J-C, Yoo K-H. A carbon nanotube metal semiconductor field effect transistor-based biosensor for detection of amyloid-beta in human serum. *Biosens Bioelectron*. 2013;50:345–350.
35. Chen H, Xiao M, He J, Zhang Y, Liang Y, Liu H, Zhang Z. Aptamer-functionalized carbon nanotube field-effect transistor biosensors for Alzheimer's disease serum biomarker detection. *ACS Sens*. 2022;7(7):2075–2083.
36. Kuo C-J, Chiang H-C, Tseng C-A, Chang C-F, Ulaganathan RK, Ling T-T, Chang Y-J, Chen C-C, Chen Y-R, Chen Y-T, et al. Lipid-modified graphene-transistor biosensor for monitoring amyloid-B aggregation. *ACS Appl Mater Interfaces*. 2018;10(15):12311–12316.
37. Salehirozveh M, Dehghani P, Zimmermann M, Roy VA, Heidari H. Graphene field effect transistor biosensors based on aptamer for amyloid-B detection. *IEEE Sensors J*. 2020;20(21):12488–12494.
38. Yu X, Sun X, Wei M, Deng S, Zhang Q, Guo T, Shao K, Zhang M, Jiang J, Han Y. Innovative multivariable model combining MRI radiomics and plasma indexes predicts Alzheimer's disease conversion: Evidence from a 2-cohort longitudinal study. *Research*. 2024;7:0354.
39. Wang Q, Ai Z, Guo Q, Wang X, Dai C, Wang H, Sun J, Tang Y, Jiang D, Pei X. Photo-enhanced chemo-transistor platform for ultrasensitive assay of small molecules. *J Am Chem Soc*. 2023;145(18):10035–10044.
40. Schedin F, Geim AK, Morozov SV, Hill EW, Blake P, Katsnelson MI, Novoselov KS. Detection of individual gas molecules adsorbed on graphene. *Nat Mater*. 2007;6(9): 652–655.
41. Suvarnaphaet P, Pechprasarn S. Graphene-based materials for biosensors: A review. *Sensors*. 2017;17(10):2161.
42. Wood JD, Wells SA, Jariwala D, Chen K-S, Cho E, Sangwan VK, Liu X, Lauhon LJ, Marks TJ, Hersam MC. Effective passivation of exfoliated black phosphorus transistors against ambient degradation. *Nano Lett*. 2014;14(12):6964–6970.
43. Zhang M, Yang L, Wu X, Wang J. Black phosphorus for photonic integrated circuits. *Research*. 2023;6:0206.
44. Zhen XV, Swanson EG, Nelson JT, Zhang Y, Su Q, Koester SJ, Bühlmann P. Noncovalent monolayer modification of graphene using pyrene and cyclodextrin receptors for chemical sensing. *ACS Appl Nano Mater*. 2018;1(6):2718–2726.
45. Kwong Hong Tsang D, Lieberthal TJ, Watts C, Dunlop IE, Ramadan S, del Rio HAE, Klein N. Chemically functionalised graphene FET biosensor for the label-free sensing of exosomes. *Sci Rep*. 2019;9(1):13946.
46. Wang H, Gao S, Zhang F, Meng F, Guo Z, Cao R, Zeng Y, Zhao J, Chen S, Hu H. Repression of interlayer recombination by graphene generates a sensitive nanostructured 2D vdW heterostructure based photodetector. *Adv Sci*. 2021;8(15):Article e2100503.
47. Seo G, Lee G, Kim MJ, Baek S-H, Choi M, Ku KB, Lee C-S, Jun S, Park D, Kim HG, et al. Rapid detection of Covid-19 causative virus (SARS-CoV-2) in human nasopharyngeal swab specimens using field-effect transistor-based biosensor. *ACS Nano*. 2020;14(4):5135–5142.
48. Liu J, Chen X, Wang Q, Xiao M, Zhong D, Sun W, Zhang G, Zhang Z. Ultrasensitive monolayer Mos_2 field-effect transistor based DNA sensors for screening of down syndrome. *Nano Lett*. 2019;19(3):1437–1444.
49. Xu S, Zhan J, Man B, Jiang S, Yue W, Gao S, Guo C, Liu H, Li Z, Wang J. Real-time reliable determination of binding kinetics of DNA hybridization using a multi-channel graphene biosensor. *Nat Commun*. 2017;8(1):14902.
50. Kesler V, Murmann B, Soh HT. Going beyond the Debye length: Overcoming charge screening limitations in next-generation bioelectronic sensors. *ACS Nano*. 2020;14(12):16194–16201.
51. Huang Y-W, Wu C-S, Chuang C-K, Pang S-T, Pan T-M, Yang Y-S, Ko F-H. Real-time and label-free detection of the prostate-specific antigen in human serum by a polycrystalline silicon nanowire field-effect transistor biosensor. *Anal Chem*. 2013;85(16):7912–7918.
52. Li J, Ni W, Jin D, Yu Y, Xiao M-M, Zhang Z-Y, Zhang G-J. Nanosensor-driven detection of neuron-derived exosomal $A\beta_{42}$ with graphene electrolyte-gated transistor for Alzheimer's disease diagnosis. *Anal Chem*. 2023;95(13):5719–5728.
53. Ninket S, Pakapongpan S, Plongthongkum N, Namchaiw P, Poo-arporn R. Molecularly imprinted polymer (MIP)-based electrochemical sensor for determination of amyloid B-42 in Alzheimer's. *Int J Chem Eng Appl*. 2023;14(3).
54. Li M, Zeng Y, Huang Z, Zhang L, Liu Y. Vertical graphene-based printed electrochemical biosensor for simultaneous detection of four Alzheimer's disease blood biomarkers. *Biosensors*. 2023;13(8):758.
55. Sheng M, Yu L, Peng Y, Wang Q, Huang J, Yang X. Combination of ternary electrochemiluminescence system of BNQDs/AgMOG-$K_2S_2O_8$ and electrochemiluminescence resonance energy transfer strategy for ultrasensitive immunoassay of amyloid-β protein. *Anal Chem*. 2023;96(1):41–48.
56. Ding M, Niu H, Guan P, Hu X. Molecularly imprinted sensor based on poly-O-phenylenediamine-hydroquinone polymer for B-amyloid-42 detection. *Anal Bioanal Chem*. 2023;415(8):1545–1557.
57. Zhou J, Sun Y, Zhang J, Luo F, Ma H, Guan M, Feng J, Dong X. Dumbbell aptamer sensor based on dual biomarkers for early detection of Alzheimer's disease. *ACS Appl Mater Interfaces*. 2023;15(13):16394–16407.
58. Jia Z, Maghaydah Y, Zdanys K, Kuchel GA, Diniz BS, Liu C. CRISPR-powered aptasensor for diagnostics of Alzheimer's disease. *ACS Sens*. 2024;9(1):398–405.
59. Zhang Y, Meng S, Ding J, Peng Q, Yu Y. Transition metal-coordinated graphitic carbon nitride dots as a sensitive and facile fluorescent probe for beta-amyloid peptide detection. *Analyst*. 2019;144(2):504–511.
60. Liu T-C, Lee Y-C, Ko C-Y, Liu R-S, Ke C-C, Lo Y-C, Hong P-S, Chu C-Y, Chang C-W, Wu P-W. Highly sensitive/selective 3D nanostructured immunoparticle-based interface on a multichannel sensor array for detecting amyloid-beta in Alzheimer's disease. *Theranostics*. 2018;8(15):4210–4225.
61. Hu T, Lu S, Chen C, Sun J, Yang X. Colorimetric sandwich immunosensor for aβ (1-42) based on dual antibody-modified gold nanoparticles. *Sensors Actuat B*. 2017;243: 792–799.
62. Zhang L, Yang C, Li Y, Niu S, Liang X, Zhang Z, Luo Q, Luo H. Dynamic changes in the levels of amyloid-B42 species in the brain and periphery of APP/PS1 mice and their significance for Alzheimer's disease. *Front Mol Neurosci*. 2021;14:723317.

63. Cao A, Mescher M, Bosma D, Klootwijk JH, Sudhölter EJ, Smet LC. Ionophore-containing siloprene membranes: Direct comparison between conventional ion-selective electrodes and silicon nanowire-based field-effect transistors. *Anal Chem*. 2015;87(2):1173–1179.
64. Kang H, Wang X, Guo M, Dai C, Chen R, Yang L, Wu Y, Ying T, Zhu Z, Wei D, et al. Ultrasensitive detection of SARS-CoV-2 antibody by graphene field-effect transistors. *Nano Lett*. 2021;21(19):7897–7904.
65. Kim BJ, Jang H, Lee S-K, Hong BH, Ahn J-H, Cho JH. High-performance flexible graphene field effect transistors with ion gel gate dielectrics. *Nano Lett*. 2010;10(9):3464–3466.
66. Wang L, Wang X, Wu Y, Guo M, Gu C, Dai C, Kong D, Wang Y, Zhang C, Qu D, et al. Rapid and ultrasensitive electromechanical detection of ions, biomolecules and SARS-CoV-2 RNA in unamplified samples. *Nat Biomed Eng*. 2022;6(3):276–285.
67. Wang X, Kong D, Guo M, Wang L, Gu C, Dai C, Wang Y, Jiang Q, Ai Z, Zhang C, et al. Rapid SARS-CoV-2 nucleic acid testing and pooled assay by tetrahedral DNA nanostructure transistor. *Nano Lett*. 2021;21(22):9450–9457.
68. Dai C, Liu Y, Wei D. Two-dimensional field-effect transistor sensors: The road toward commercialization. *Chem Rev*. 2022;122(11):10319–10392.